J. Fluid Mech. (1969), *vol.* 38, *part* 4, *pp.* 721–742
Printed in Great Britain

Stability and dynamics of rotating dielectrophoretic equilibria

By R. T. CALVERT AND J. R. MELCHER
Department of Electrical Engineering, Massachusetts Institute of Technology, Cambridge, Massachusetts

(Received 14 November 1968)

In the design of dielectrophoretic liquid orientation and expulsion systems for zero-gravity environments, maximum electromechanical effect of an imposed electric field is obtained by concentrating the field gradients in the neighbourhood of liquid interfaces. In typical configurations, the electric field gradient plays the role of an electromechanical wall, with a stiffness and inertia represented dynamically by electrohydrodynamic surface waves. As an orientation system rotates, the liquid motions are characterized by these waves as they couple to inertial bulk oscillations and centrifugal surface waves resulting from the rotation. A study is made of configurations typified by an equilibrium in which a circular cylindrical column of inviscid liquid undergoes rigid body rotation. The equilibrium is made possible, even though the cylindrical interface is bounded from outside only by its vapour, because the interface is stressed by an essentially tangential axial electric field intensity, with a strong gradient in the radial direction. Dispersion equations are developed for the electrohydrodynamic centrifugal waves of small amplitude. Conditions for incipience of instability and the frequencies of normal modes of oscillation are given. Experimental observations, which demonstrate the destabilizing influence of the rotation and the effect of rotation and electric field intensity on the normal mode frequencies, are in satisfactory agreement with the theory.

1. Introduction

Background; electrohydrodynamics

The electrohydrodynamics of perfectly insulating polarized liquids has received considerable attention because of its possibilities for solving problems of cryogenic fluid management in the weightless environments of space. The electric field is used to replace the influence of gravity through the agent of the Korteweg–Helmholtz force density (Stratton 1941, p. 145).

$$\mathbf{F} = -\tfrac{1}{2}\mathbf{E}.\mathbf{E}\nabla\epsilon, \tag{1}$$

where $\mathbf{E}$ and ϵ are the electric field intensity and permittivity, respectively. This is the 'dielectrophoretic' force density that remains in a classical liquid if there is no space charge, and if only the incompressible dynamics are of interest, so that the electrostriction force density makes no observable contribution (Melcher

1963, p. 23). In systems of homogeneous fluids, (1) makes it clear that electromechanical coupling is limited to interfaces, where ϵ suffers an abrupt discontinuity. Hence, in the case in which **E** is tangential to an interface between a liquid and its vapour, there is a surface force density normal to the interface from liquid to vapour, given by

$$T_e = \tfrac{1}{2}E^2(\epsilon - \epsilon_0), \tag{2}$$

where ϵ_0 is the permittivity of free space.

Thus it is that the dynamics of electrohydrodynamic surface waves play a fundamental role in dielectrophoretic fluid mechanics.

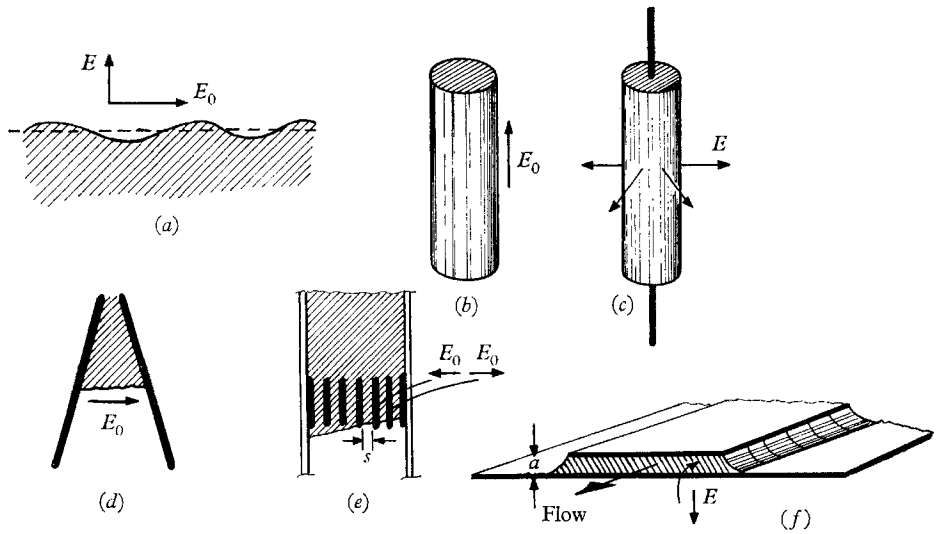

FIGURE 1. Representative static dielectrophoretic equilibria. In (*a*) and (*b*), perturbations are of a purely self-field type. In (*c*)–(*f*), imposed and self-field effects are present; in (*c*), self-field effects are destabilizing and in (*d*)–(*f*) they are stabilizing. Cases (*e*) and (*f*) are likely to be dominated by imposed-field effects because the field gradients are concentrated in the neighbourhood of the interfaces.

Some fluid field configurations that have been studied and that will help to place the present work in perspective are shown in figure 1. As the interface departs from one of the equilibria shown, it is subject to perturbation electrical surface force densities of two types: (i) 'imposed field' perturbations caused by the interface moving through a non-uniform imposed electric field, and (ii) 'self-field' perturbations created because deformations of the dielectric lead to changes in the electric field intensity at the interface which, in turn, alter the electrical surface force density.

In configuration (*a*) of figure 1, the equilibrium consists of a plane interface stressed by a uniform electric field intensity having components normal and tangential to the interface. Because the imposed field is uniform, the electrohydrodynamics are due entirely to self-field effects. It is well known that the perpendicular field tends to produce instability, while the tangential field stiffens the interface for perturbations propagating along the field lines but

has no influence on those propagating across the field lines (Melcher 1963, chapters 3 and 4). To be certain of observing these dielectrophoretic effects, it is necessary to use ac fields with frequencies much greater than the reciprocal relaxation time for free charges in the liquid (Melcher & Schwartz 1968; Devitt & Melcher 1965).

Because the imposed field is uniform, perturbations from the circular cylindrical static equilibrium of figure 1 (*b*) have the same self-field characteristics as the plane interface in a tangential field. Perturbations independent of the axial direction are unaffected by E_0, while those propagating in the axial direction are stiffened (Nayyer & Murty 1960).

By contrast, if coaxial electrodes are used to impose a radial field on a circular cylindrical equilibrium, both self-field and imposed field effects are present. The self-field effects, as in the case of the plane interface in a perpendicular field, tend to produce instability; the imposed field effects, however, are stabilizing, because the imposed field (hence the radially directed surface force density) decays with radial distance. Thus, in configuration (*c*) of figure 1, a modest electric field tends to make the equilibrium shown stable, but a large electric field produces instability (Reynolds 1965).

Because of the inherent tendency toward self-field-induced instability caused by a normal electric field intensity, dielectrophoretic liquid orientation and expulsion systems are designed to take advantage of fields imposed tangential to the interface. However, because there is no self-field interaction between the field and those perturbations with hills and valleys parallel to the lines of electric field intensity, it is necessary to engineer appropriate gradients in the imposed fields for purposes of stabilization.

The essence of a field-gradient-stabilized system is shown in figure 1 (*d*). The field experienced by the interface decreases as a portion of the liquid falls. Thus, the tendency is for the equilibrium shown to be retained because there is an attendant decrease in the downward-directed surface force density (equation (2)). Note that the dielectrophoretic surface force density does not 'hold' the liquid in place, but rather that the system is arranged so that hydrostatic pressure maintains the static equilibrium. The electric field serves only to stabilize the equilibrium (Melcher & Hurwitz 1967).

In configuration (*e*) of figure 1, the field gradient stabilization is carried to the extreme by concentrating it in the neighbourhood of the interface. The field gradient is at once confined within a distance from the electrode edges on the order of the plate spacing, s, and for a given E_0 made inversely proportional to s. Thus, at the expense of confining the region of interaction, it is possible to make s sufficiently small that the imposed-field effects dominate those due to the self-fields. Moreover, this type of arrangement makes it possible to carry out liquid vapour experiments dominated by electrohydrodynamic forces even in static, earth-bound tests (Melcher, Guttman & Hurwitz 1968).

Concentrated field configurations are the basis not only for the achievement of stable static equilibria, but also for slosh control (Melcher, Guttman & Hurwitz 1968) and flow confinement (Melcher, Hurwitz, Fax & Blutt 1968). This latter case is sketched as (*f*) of figure 1, where flow is between a ribbon electrode

at high potential with respect to a tank wall. Two of the 'dielectrophoretic pipe' walls are electromechanical, allowing ingestion of adjacent liquid, but preventing its expulsion in any direction except that of flow. The electric field plays the same role with respect to these lateral walls as gravity plays in free-surface channel flows. Thus, electrohydrodynamic surface waves propagating on the walls of the 'pipe' are important in the same way that gravity waves are essential in free channel flows (Rouse 1946, pp. 132–47). If the ribbon-wall spacing (a) is small compared to wavelengths of interest, the self-field effects are negligible compared to the effects of the imposed concentrated-gradient field. The following sections describe an investigation into the nature of similar waves but with the fluid assuming a steady, rigid-body equilibrium rotation.

Previous investigations (Grodzinsky 1967; Habip 1967; Wong 1966) concerned with the electrohydrodynamics of rotating liquids relate to the relatively small self-field effects and therefore tend to suffer from a lack of experimental evidence.

Rotational effects are important to dielectrophoretic liquid management in space vehicles subject to controlled or uncontrolled rotations. The results are also of interest in making voltage-controlled liquid gyroscopic devices. It is important to recognize that dielectrophoretic hydrodynamics is the complete analogue of ferrohydrodynamics (Cowley & Rosensweig 1967) and so developments also apply to analogous motions of a magnetized liquid.

Background: rotating fluids

As part of literature pertaining to the dynamics of rotating fluids, the following sections add yet more examples to the 'crowds of extremely interesting cases' mentioned by Lord Kelvin in his original paper on the subject (Kelvin 1910, pp. 152–65; Chandrasekhar [1961). From a basic point of view, these studies relate to the manner in which electrohydrodynamic surface waves couple to inertial waves with gyration frequency $2\,\Omega$, in the bulk of the liquid, where Ω is the angular velocity of rotation (Chandrasekhar 1961, pp. 85–86). In view of the Taylor-Proudman theorem (Chandrasekhar 1961, pp. 83–85, 87) it is not surprising that instability manifests itself as overstability.

In the limit of an extremely large electric field intensity, the 'dielectrophoretic wall' becomes infinitely stiff and the dynamics of most of the modes reduce to the case of a fluid contained within a vessel having rigid walls and rotating at constant angular velocity. Because of previous work, the phenomenon under study might be referred to as 'dielectrophoretic elastoid-inertia oscillations and instability' (Fultz 1959). However, it is the dynamics of a rotating interface that is mainly of concern here, and a more accurate description of the phenomenon under investigation is 'dielectrophoretic-centrifugal waves and instabilities' (Phillips 1960). As will be seen, it is sometimes difficult to distinguish between inertial oscillations and surface-wave modes; they can couple and conspire to produce overstability. Recent reviews concerned with rotating fluid systems help to place this work in perspective (Bretherton *et al.* 1966, Lighthill 1966).

Equilibrium configurations

Electrodes and oriented liquid are shown in figure 2, in the two configurations (A) and (B) to be dealt with. Configuration A, the circular electrode over a second planar electrode, as shown in figure 2(a), permits experimental investigation even in the face of an axially directed gravitational acceleration, g. The electrodes constrain fluid motions to be perpendicular to the axis of rotation, with the liquid assuming an essentially circular cylindrical geometry, filling the region under

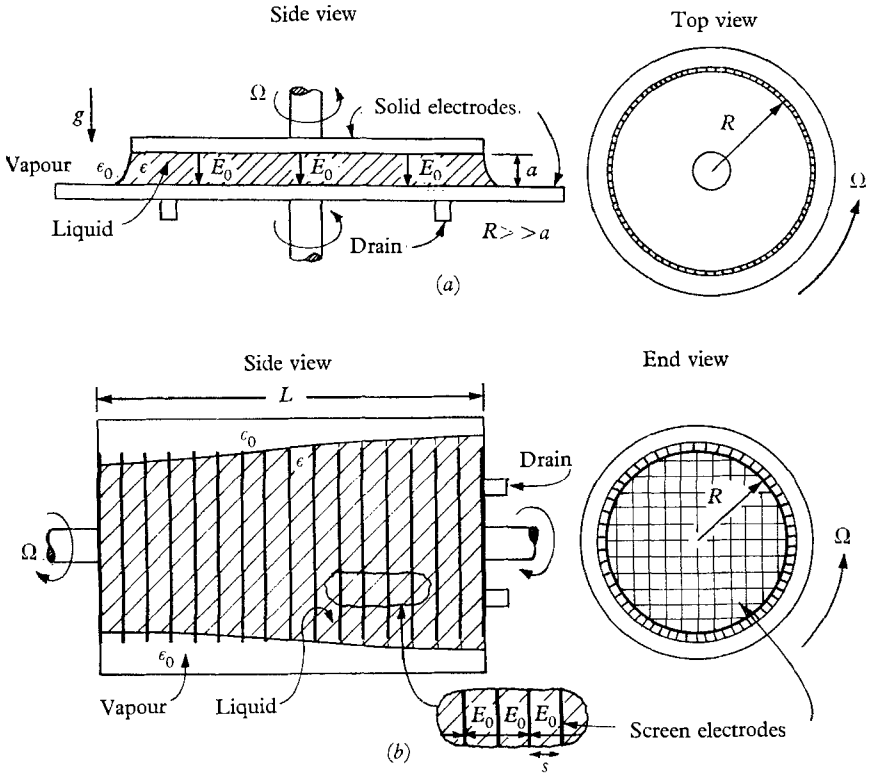

FIGURE 2. (a) Configuration A: circular electrode over a plane surface, with the fluid filling the cylindrical region between. The fringing fields tend to stabilize the circular interface, so that the equilibrium is possible even with rotation and gravity acting as shown.

(b) Configuration B: a system of circular screen electrodes orient a column of liquid with the same equilibrium radius as the electrodes. The screens permit communication of fluid between sections. Rotation is about the axis of the cylindrical structure.

the circular electrode. The interface is in the fringing field region, and hence tends to be stable even with electrodes and liquid undergoing rigid body rotation.

The equilibrium depicted in figure 2(b), configuration B, is similar, except that there are many electrodes at alternate polarities. The fringing fields in the neighbourhood of the interface at the radius R tend to stabilize the column of liquid in spite of the rigid body rotation of the entire system about the axis. The electrodes are constructed from screens that permit the communication of liquid

between sections. Thus, the motions are modelled by assuming that the screens present a negligible resistance to the motions, and serve only to impose a radial distribution of electric field intensity gradient concentrated at the radius, R.

Except for a geometric constant, the model for configuration A is a special case of B, with modes propagating along the axis of rotation ignorable.

2. Theory of dynamics

Outline

Coupling between the electric field and fluid is confined to the interface. Therefore, it is convenient to represent the mechanical and electrical bulk dynamics in terms of pressure- or stress-displacement relations at the interface. At the outset, surface perturbations are assumed to take the form

$$\xi(\theta, z, t) = \mathrm{Re}\,\hat{\xi}\exp j(\omega t - m\theta - kz). \tag{3}$$

The co-ordinates (r, θ, z, t) are measured from a frame of reference having the same angular velocity Ω as the fluid, relative to the laboratory frame.

In the following subsections, the fluid pressure as well as electrical and surface tension surface force densities are evaluated in terms of $\hat{\xi}$. The dispersion equation for waves on the interface and in the bulk follows from the condition that these radially directed surface force densities balance. That is,

$$\pi(R+\xi) - \pi_0 + T_e(R+\xi) + T_s(R+\xi) = 0, \tag{4}$$

where π, T_e and T_s are the total fluid pressure, and the electric and surface tension surface force densities, respectively. With $\xi = 0$, the equation requires that

$$\pi(R) - \pi_0 + T_e(R) + T_s(R) = 0. \tag{5}$$

Note that because $T_e > 0$, for a negligible effect of surface tension, the ambient pressure π_0 exceeds that in the interior of the fluid.

In terms of solutions having the form of (3), the perturbation amplitudes must obey the linearized expression remaining when (5) is subtracted from (4)

$$\hat{\pi} + \hat{T}_e + \hat{T}_s = 0, \tag{6}$$

where the (r, θ, z, t) dependence is removed by assuming solutions have the form of (3).

Mechanical pressure-displacement relations

In terms of the rotating frame co-ordinates, the linearized equations of motion for the fluid (with $\mathbf{i}_z$ a unit vector in the axial direction) are (Chandrasekhar 1961, pp. 83–85, 87):

$$\rho\frac{\partial \mathbf{v}}{\partial t} - 2\mathbf{v}\times\Omega\mathbf{i}_z + \nabla p = 0; \quad \pi = \tfrac{1}{2}\rho\Omega^2 r^2 + p + \Pi, \tag{7}$$

$$\nabla . \mathbf{v} = 0. \tag{8}$$

Thus, viscosity and compressibility are ignored. The total pressure π includes the perturbation pressure, p, and a constant, Π, determined by the equilibrium boundary conditions at the interface and the ambient pressure.

If solutions to (7) and (8) are assumed in the form $\mathrm{Re}\,\hat{p}(r)\exp j(\omega t - m\theta - kz)$, (7) and (8) require that for $\omega \neq 2\Omega$,

$$r^2D^2\hat{p} + rD\hat{p} - \hat{p}(m^2 + r^2k^2\Delta^2) = 0, \tag{9}$$

where $\Delta^2 \equiv 1-(2\Omega/\omega)^2$, $D(\ ) = d(\ )/dr$, and

$$\hat{v}_r = j[\omega D\hat{p} - 2m\Omega(\hat{p}/r)]/\rho\omega^2\Delta^2. \tag{10}$$

In configuration A, the spacing (a) is sufficiently small to warrant ignoring the dependence of ξ on the axial direction, z. What variations exist in the interface position with z are quasi-static in nature in that the profile is essentially independent of the dynamics. Thus, the balance of surface forces in this case is taken as independent of z, and represented by an average over the z dimension of the interface. As far as the mechanical motions are concerned, this means that $k = 0$, and the appropriate solution to (9) that is not singular at the origin is,

$$\hat{p}(r) = \rho R(\omega^2 + 2\omega\Omega)\,\hat{\xi}(r/R)^m/m. \tag{11}$$

In the case of figure 2(b), the interfacial axial wavelengths $2\pi/k$ are also long compared to the plate spacing, s, but it is appropriate to include their effects. The non-singular solution to (9) for this case is

$$\hat{p}(r) = \rho\omega^2 R\left[\frac{-2m\Omega}{\omega\Delta^2}J_m(jkR\Delta) + \frac{jkR}{\Delta}J'_m(jkR\Delta)\right]^{-1}\hat{\xi}J_m(jkr\Delta) \tag{12}$$

with J_m the mth order Bessel function of first kind.

The constants in these last two solutions have been adjusted so that $\hat{v}_r(r)$, as given by (10), satisfies the condition $\hat{v}_r(R) = j\omega\hat{\xi}$. Finally, the complex amplitude of the total pressure π evaluated at the deformed position of the interface follows from (7) as

$$\hat{\pi}(R+\xi) = \rho\Omega^2R\hat{\xi} + \hat{p}(R), \tag{13}$$

where $\hat{p}$ is given by (11) or (12), whichever case is under consideration.

Electrical stress-displacement relations

In the limit where self-field effects dominate, a simple model gives a surprisingly good description of the electrical surface force density. As the interface passes from the region between the electrodes, where the electric field intensity is E_0, to the field-free region beyond, the surface force density of (2) varies from a maximum of $(\epsilon-\epsilon_0)E_0^2/2$ to zero, as shown in figure 3. The field decay is represented to a good approximation by the piecewise continuous model of figure 3, which represents the variation as being linear over the range $R - s/2 < \xi < R + \frac{1}{2}s$, and constant elsewhere (Melcher, Guttman & Hurwitz 1968; Melcher, Hurwitz, Fax & Blutt 1969; Guttman 1967).

The variation of T_e shown in figure 3 pertains to the case in which the field is imposed by electrodes, each with an edge at $r = R$. Thus it applies directly to configuration B, figure 2(b), and for small perturbations from equilibrium $(|\hat{\xi}| < \frac{1}{2}s)$, the required dependence of $\hat{T}_e$ on $\hat{\xi}$ is simply

$$\hat{T}_e = -\tfrac{1}{2}(\epsilon-\epsilon_0)E_0^2(\hat{\xi}/s). \tag{14}$$

However, with configuration A, the lower electrode extends beyond the fringing field region and assumes the position of the symmetry plane shown in figure 3. It follows that in the case of figure 2(*a*), the appropriate dependence of T_e is given by (14) with $s \to 2a$.

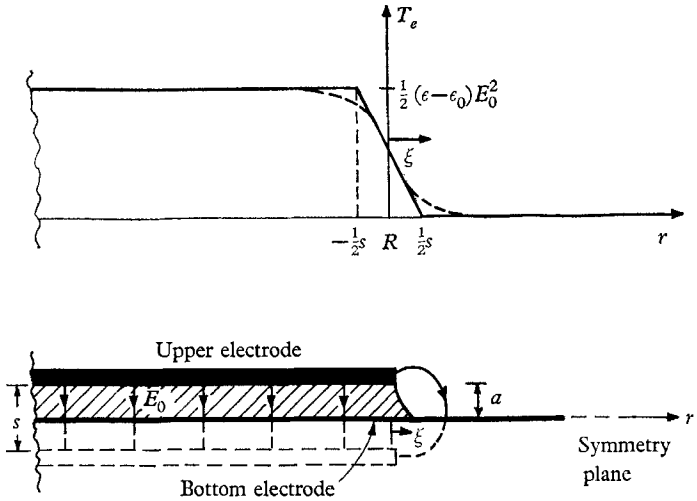

FIGURE 3. Electric surface force density T_e experienced by the interface as a function of radial position, ξ.

In this latter case (figure 2(*a*)), the surface force density represents an average over the axial length; the plane motion model ignores the axial dependence of the interface position.

Effects of surface tension

The influence of surface tension is included as a correction, rather than a first-order effect. In general, it depends on the manner in which the liquid wets the electrodes. If the interface was composed simply of a circular cylindrical column, with no electrodes to which to attach, the additional surface force density would be (Lamb 1932, p. 473)

$$T_s = T\left(-\frac{1}{R}+\frac{\xi}{R^2}+\frac{1}{R^2}\frac{\partial^2\xi}{\partial\theta^2}+\frac{\partial^2\xi}{\partial z^2}\right), \tag{15}$$

where T is the surface tension.

In configuration A of figure 2, the interface is observed to remain attached to the edge of the upper electrode. Transverse motions are accommodated because the lower electrode allows the interface to slosh unobstructed in and out. In static equilibrium, the interface assumes a profile varying from that sketched in figure 2(*a*) to a nearly perpendicular straight line, depending on the amount of fluid oriented by the field, and on the field strength relative to that of gravity. With the vertical equilibrium, motions lead to a profile that is somewhat sinusoidal, with wavelength $4a$. Thus, the approximation is made that

$$\xi(\theta,z,t) = \xi(\theta,t)\sin(2\pi z/Na), \tag{16}$$

where N, the number of quarter wavelengths in the axial distance a, is 4. With the interface extending out from under the upper electrode, its extent between

electrodes exceeds a, and it is expected that N in (16) should be taken as somewhat larger than 4. Thus, the z-dependence in (15) is fixed by making k in (3) $2\pi/Na$. Substitution of (3) into (15) then gives

$$\hat{T}_s = T\left[1-m^2-\left(\frac{2\pi}{N}\right)^2\left(\frac{R}{a}\right)^2\right]\hat{\xi}/R^2 \tag{17}$$

for configuration A.

In the case of figure 2(b), it is expected that, as the interface moves past the edges of the electrodes, initially it tends to attach, but finally breaks away. Thus, there is an effective surface force density due to surface tension which has a non-linear dependence on $\hat{\xi}$ similar to that of T_e'; somewhat as depicted by figure 3. Here, interest is confined to the secondary effects of surface tension in experiments having the configuration of figure 2(a), and the effects of surface tension are ignored in the case of figure 2(b).

Dispersion equations

Radial interfacial force equilibrium as required by (6) can now be expressed with terms linear in the arbitrary amplitude $\hat{\xi}$. The resulting expressions, which are homogeneous in $\hat{\xi}$, are in general satisfied only if the coefficients of $\hat{\xi}$ vanish. Thus, (6), (11), (13), and (14), (with $s \to 2a$) and (17) give the dispersion equation for configuration A:

$$\omega^2[\rho R]+\omega[2\rho\Omega R]+m\left[\rho\Omega^2 R-\frac{(\epsilon-\epsilon_0)E_0^2}{4a}+\frac{T}{R^2}\left(1-m^2-\frac{4\pi^2R^2}{N^2a^2}\right)\right]=0. \tag{18}$$

Of course, conservation of mass requires that $m \neq 0$.

Similarly, (6), (12), (13) and (14) combine to give the dispersion equation for configuration B.

$$D_p(\omega,m,k)+\left[\rho\Omega^2R-\frac{(\epsilon-\epsilon_0)E_0^2}{2s}\right]=0, \tag{19}$$

where

$$D_p(\omega,m,k) \equiv \frac{\rho\omega^2 J_m(jkR\Delta)}{-\frac{2m\Omega}{\omega\Delta^2R}J_m(jkR\Delta)+\frac{jk}{\Delta}J'_m(jkR\Delta)}.$$

The main complication of the rotation, the dependence of Δ [defined with (9)] on ω, is familiar from many problems concerned with inertial oscillations (Habip 1967; Chandrasekhar 1961; Fultz 1959; Phillips, 1960; Bretherton *et al.* 1966).

3. Azimuthal modes (configuration A)

Natural frequencies

The purely azimuthal modes represented by (18) are conveniently studied because of the simple quadratic dependence of the rotation on ω. With the frequency of the mth mode without rotation defined as

$$\omega_m=\left\{\frac{m(\epsilon-\epsilon_0)E_0^2}{4a\rho R}+\frac{mT}{\rho R^3}\left[\left(\frac{2\pi R}{Na}\right)^2+m^2-1\right]\right\}^{\frac{1}{2}}, \tag{20}$$

(18) shows that the natural frequencies exhibit a splitting characteristic of the effect of rotation

$$\omega=-\Omega\pm[\Omega^2(1-m)+\omega_m^2]^{\frac{1}{2}} \quad (m=1,2,3,\ldots). \tag{21}$$

Experimental observations of similar but purely hydrodynamic modes obtained on the interface between a cylindrical column of air and a surrounding, rotating liquid (Philips 1960) have been successfully correlated with a dispersion equation having a form similar to (21). In that case, with the heavier liquid on the outside, rotation tended to augment the stability.

As must be expected for an equilibrium like that considered here, one that places the heavy liquid 'on top of' the lighter, surrounding gas, the effect of the rotation on all but the $m = 1$ mode is to produce instability. Further, this tendency for instability caused by rotational forces is in competition with the forces that contribute to ω_m, which, in the absence of surface tension, is in direct proportion to the imposed electric field intensity.

Instability

For purposes of determining the critical field intensity E_c for incipience of instability, as well as the critical mode number m_c at which the instability first occurs as E_0 is reduced, it is convenient to write the dispersion equation (21) in the form

$$\bar{\omega} = (\omega/\Omega) = -1 \pm [1 + m(\Gamma - 1) + m\alpha(\beta + m^2 - 1)]^{\frac{1}{2}}, \tag{22}$$

where $$\Gamma = \frac{(\epsilon - \epsilon_0) E_0^2}{4 a \rho \Omega^2 R}, \quad \alpha = \frac{T}{\rho \Omega^2 R^3} \quad \text{and} \quad \beta = (2\pi R/Na)^2.$$

Instability sets in as the bracketed term of (22) goes to zero. As this occurs, $\bar{\omega} = -1$ and the equilibrium is overstable in the rotating frame of reference.

If $R \gg a$, then $\beta \gg 1$, and from (22) the condition of marginal instability is

$$\Gamma = \Gamma(E_0) = 1 - (1/m) - \alpha(m^2 + \beta). \tag{23}$$

Consider that the angular velocity Ω has been established at a particular value and E_0 set to make the equilibrium stable. Then, as E_0 is decreased through the critical value E_c, such that $\Gamma = \Gamma_c$, the electric perturbation surface force density can no longer balance the perturbation rotational forces and the equilibrium becomes unstable.

The maximum of (23) is Γ_c, and occurs at the critical mode number m_c. Because of the closed circular nature of the surface, the mode number m must be an integer, thus

$$m_c = \text{the closest integer to } (2\alpha)^{-\frac{1}{2}}. \tag{24}$$

However, in most situations, m is large and the influence of its discrete nature on the conditions for instability can be ignored. Substitution of (24) into (23) then yields the critical parameter Γ_c, and hence the critical electric field intensity E_c:

$$E_c^2 = \frac{4a}{\epsilon - \epsilon_0}\left[\rho R \Omega^2 - G T^{\frac{1}{3}} (\rho \Omega^2)^{\frac{2}{3}} - \frac{4\pi^2 T}{N^2 a^2}\right], \tag{25}$$

where $G = 2^{\frac{1}{3}} + (\frac{1}{2})^{\frac{2}{3}} \simeq 1{\cdot}9$. For $E_0 > E_c$ the system is stable.

4. Axial modes (configuration B)

Natural frequencies

By contrast with the two-dimensional (azimuthal) modes considered in §3, three-dimensional modes are represented by an eigenvalue equation (19), which is difficult to deal with. It assumes the normalized form

$$4\Delta^2\{[1-\Delta^2][\mp m\sqrt{(1-\Delta^2)}+jk\Delta RJ'_m(jk\Delta R)/J_m(jk\Delta R)]\}^{-1} = \Gamma - 1, \qquad (26)$$

where now $\Gamma = (\epsilon - \epsilon_0)E_0^2/2s\rho\Omega^2 R$ and

$$\bar{\omega} = \pm 2[1-\Delta^2]^{-\frac{1}{2}}. \qquad (27)$$

The upper and lower signs in (26) and (27) are to be identified with each other, and will be referred to as branches 1 and 2, respectively.

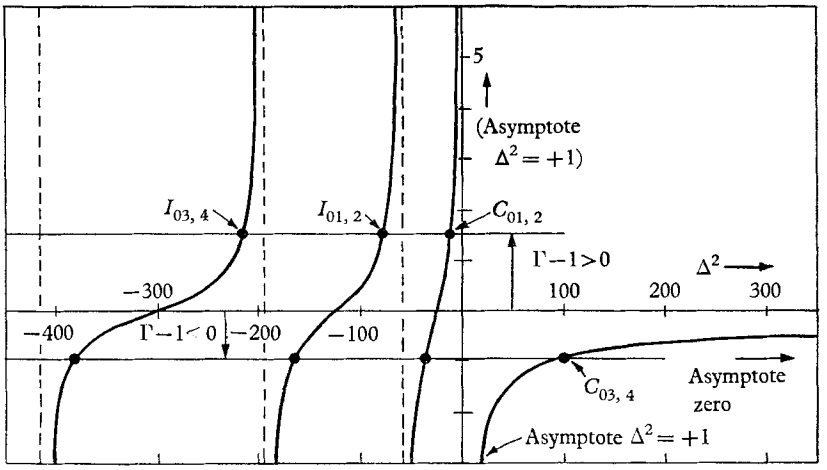

FIGURE 4. Graphic representation of the roots to (26) which are either purely imaginary or real. Branches 1 and 2 are degenerate, so that each solution for Δ^2 represents two eigenfrequencies; $kR = 0{\cdot}5$ and $m = 0$. The corresponding eigenfrequencies are given in figure 5.

The $m = 0$ modes represent a special case, in that the branches of (26) are then identical. For real values of Δ^2, solutions to (26) are conveniently pictured by plotting the left side of (26) as a function of Δ^2. Roots are those values of the abscissa in which the plot has the ordinate $\Gamma - 1$. As an example, figure 4 shows the case where $kR = 0{\cdot}5$. Each root corresponds to two eigenfrequencies, as given by (27), hence to two modes.

Most of the modes can be associated with inertial oscillations such as would exist in the bulk of the liquid even if the interface was constrained by a rigid wall. These are identified as I_{0j} in figure 4, and as the electric field is made very large ($\Gamma \to \infty$), they have eigenfrequencies that increase asymptotically, approaching those for the case of inertial oscillations in a rigid circular container. The remaining modes are denoted by C_{0j} to indicate that they are at least associated with electrohydrodynamic centrifugal waves of the type discussed in §3. By contrast with the inertial modes, the eigenfrequencies of the modes $C_{01,2}$ approach $\pm\infty$

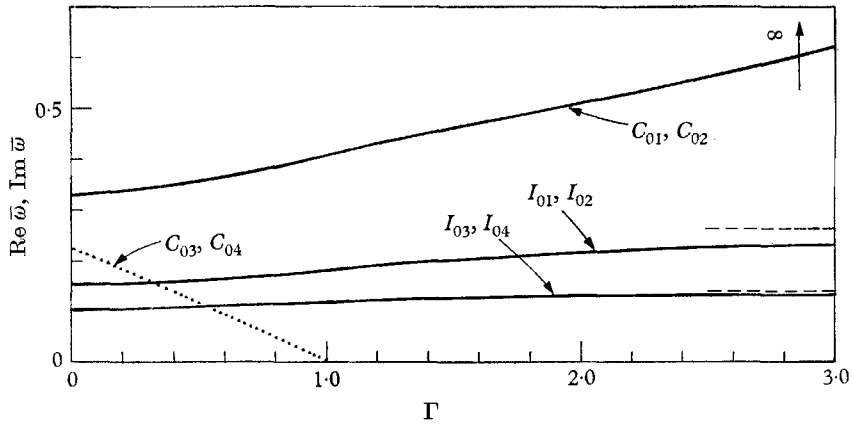

FIGURE 5. Eigenfrequencies for $m = 0$ modes with $kR = 0{\cdot}5$ as a function of the normalized applied electric field intensity. For $\Gamma < 1$, the centrifugal modes C_{03} and C_{04} display a purely exponential growth, with the growth rate going to zero at $\Gamma \to 0$. The frequencies of mode pairs are negative. ——, Re $\bar{\omega}$; – – – –, Im $\bar{\omega}$.

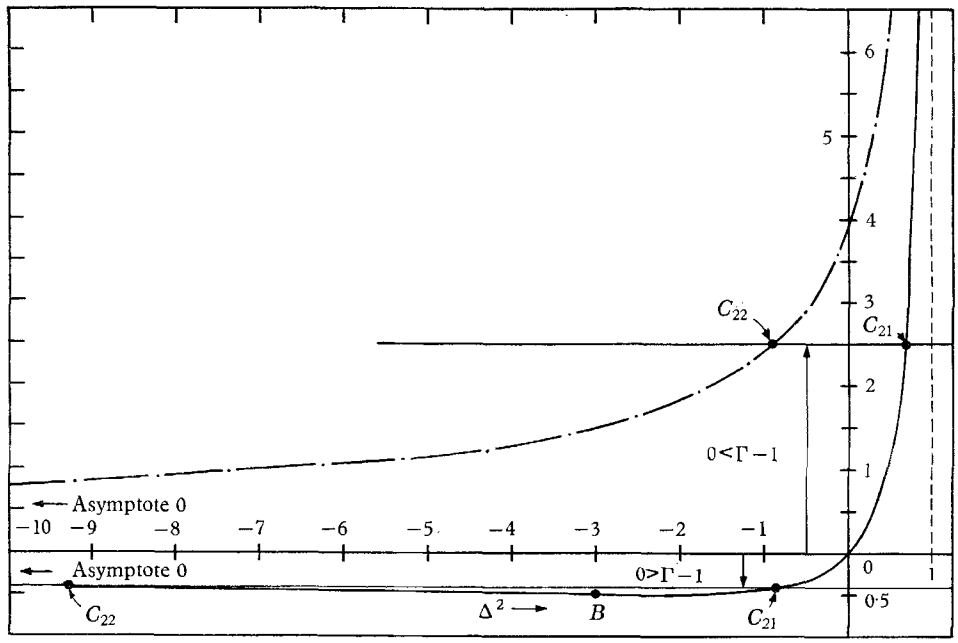

FIGURE 6. Long-wave limit of (26) for $m = 2$ modes. This characterizes those modes $m > 1$ and allows an identification of the eigenfrequencies in terms of the branches of (26) in the limit where the inertial oscillations are suppressed ($kR \to 0$). —·—·—, branch 1; ———, branch 2.

as $\Gamma \to \infty$. For $\Gamma < 1$, two additional modes, $C_{03,4}$, appear for real values of $\Delta^2 > 0$ and from (27) it is clear that these are unstable. The positive eigenfrequencies are shown in figure 5 for the case of figure 4.

As is typical of inertial oscillations, eigenfrequencies approach zero with increasing mode number. Hence there are an infinite number of modes having frequencies within some neighbourhood of zero. As $\Gamma \to 1$, the unstable modes $C_{03,4}$ have growth rates that approach zero; these modes join the infinite number having frequencies in the neighbourhood of $\omega = 0$.

In the long-wave limit ($kR \to 0$), the modes $m \neq 0$ approach those discussed in §3 (with Γ suitably redefined by identifying $s \to 2a$). It is helpful in understanding the finite kR case to consider this long-wave limit in terms of a plot analogous to that of figure 4. As $kR \to 0$, the $m = 2$ modes are represented by the plot of figure 6. Now, the branches of (26) are not degenerate. For $\Gamma < 1$, branch 2 accounts for both modes C_{21} and C_{22}, while for $\Gamma > 1$, C_{22} is given as a root of branch 1. Combining the long-wave limit of (26) with (27) gives the eigenfrequencies of the mth modes $C_{m1,2}$ as

$$\bar{\omega} = -1 \pm [1 + m(\Gamma - 1)]^{\frac{1}{2}}. \tag{28}$$

The eigenfrequencies illustrated in figure 7 are drawn for the $m = 2$ modes using figure 6, but can also be obtained from (28) which holds for any mode $m \neq 0$ in the limit $kR \to 0$. Note that overstability results as Γ is decreased below 0·5, with the roots joining at B in figures 6 and 7, and then represented by complex values of Δ^2. In the long-wave limit these complex values of Δ^2 are easily found because the Bessel's functions can be represented by polynomials. But, with kR finite, the problem of finding modes with Δ^2 complex requires solving (26) with Bessel's functions of a complex argument. Fortunately, most of the modes are represented by roots of (26) having real values of Δ^2, with graphical solutions illustrated in figure 8 for the case $kR = 0{\cdot}5$.

The effect of a finite kR is to make evident an infinite set of inertial modes I_{mj} which in the characteristic manner decrease in frequency magnitude as the mode number increases. As for the $m = 0$ modes, the effect of raising the electric field intensity is to increase the inertial oscillation frequencies. The frequencies of the first two inertial modes are shown in figure 9 as functions of the normalized electric pressure, Γ.

Although solutions labelled $C_{2,1-4}$ are denoted by a C for centrifugal modes, examination shows that these four have properties of both the inertial and the centrifugal modes; they are of a hybrid character. With $\Gamma = 0$, modes C_{22} and C_{24} are oscillatory, while modes C_{23} and C_{21} combine to give overstabilities and underdamped modes. As Γ is raised, this latter pair of modes join at B in figure 8 and become oscillatory. However, with a further increase in Γ, point A is reached and modes C_{23} and C_{24} join to become underdamped and overstable. Solution for the eigenfrequencies of these last two modes beyond this level of Γ requires numerical solution of (26) with Δ^2, and hence the frequency, complex. Of course, Δ^2 is also complex for the $C_{21,3}$ modes with Γ below point B, but small argument approximations of the Bessel's functions make it possible to find these roots analytically.

The frequencies for the four C modes are shown in figure 9. Note that the over-

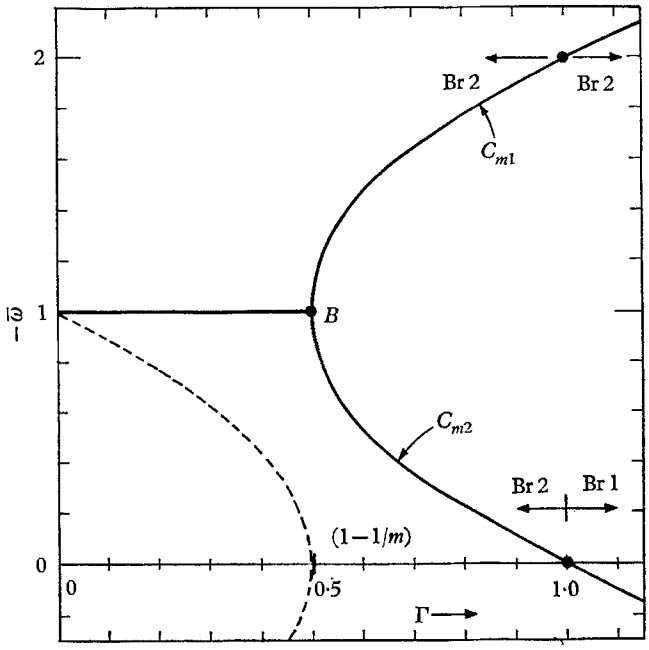

FIGURE 7. Eigenfrequencies for modes $m \neq 0$, $kR \to 0$. The particular numbers are for the $m = 2$ modes, but the plot characterizes higher order modes. ———, $\bar{\omega}_r$; – – – –, $\bar{\omega}_i$.

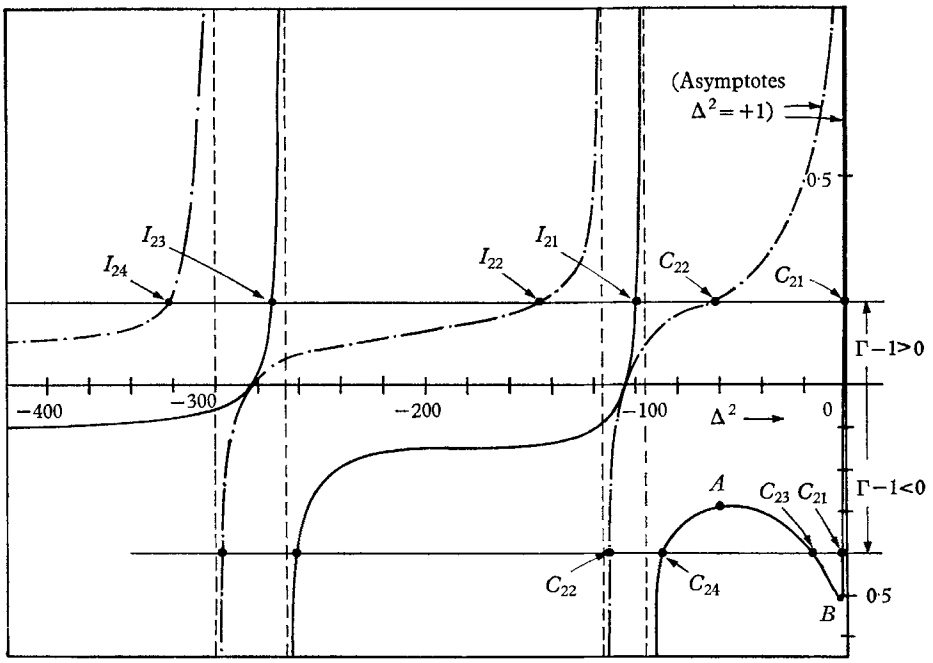

FIGURE 8. Graphic representation of roots of (26) which are either purely real or imaginary. $kR = 0{\cdot}5$ and $m = 2$. Modes C_{23} and C_{21} switch from overstable to stable at B as Γ is raised, while C_{23} and C_{24} become overstable at A as Γ is raised still further. —·—·—·—, branch 1; ———, branch 2.

stability caused by raising Γ beyond point A has a growth rate, and oscillation rate that approaches zero as $\Gamma \to 1$. As for the unstable $m = 0$ modes, this pair joins the infinite number in the neighbourhood of zero frequency as $\Gamma \to 1$.

As Γ is increased to infinity, the modes C_{22} and C_{21} have eigenfrequency magnitudes that approach infinity, as is expected for the inertial modes as the electrohydrodynamic walls become infinitely stiff. Note, however, that the mode C_{22}

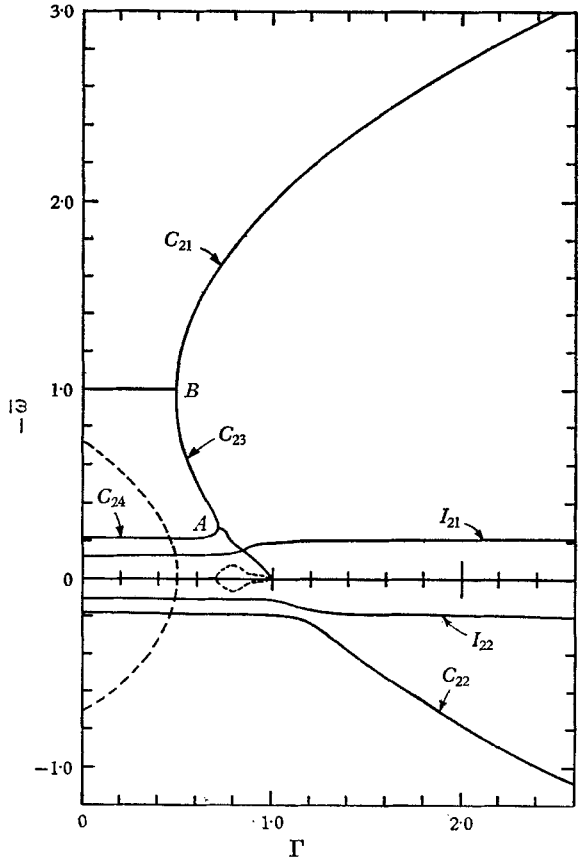

FIGURE 9. Eigenfrequencies as a function of normalized electric field intensity, showing coupling of inertial oscillations and electrohydrodynamic centrifugal waves to produce overstability at A. Points A and B are to be identified with the respective points in figure 8.

remains oscillatory throughout the full range of Γ; for $\Gamma \to 0$ it has the character of an inertial oscillation, while for $\Gamma \to \infty$, it assumes the properties of a centrifugal mode.

Although no claim is made here that all modes and all possible wavelengths $2\pi/kR$ have been examined, it appears that a sufficient condition for stability of all modes is $\Gamma > 1$. Certainly, if $\Gamma < 1$, there are modes of instability.

5. Experiments

Apparatus

In order to observe incipient instability and normal mode oscillations for configuration A (figure 2 (a)), the rotating tank and drive assembly shown in figure 10 is used. The two electrodes are brass and the upper disk is bevelled on its lower surface 0·7 of a degree from the centre to the outer rim, to minimize the collection

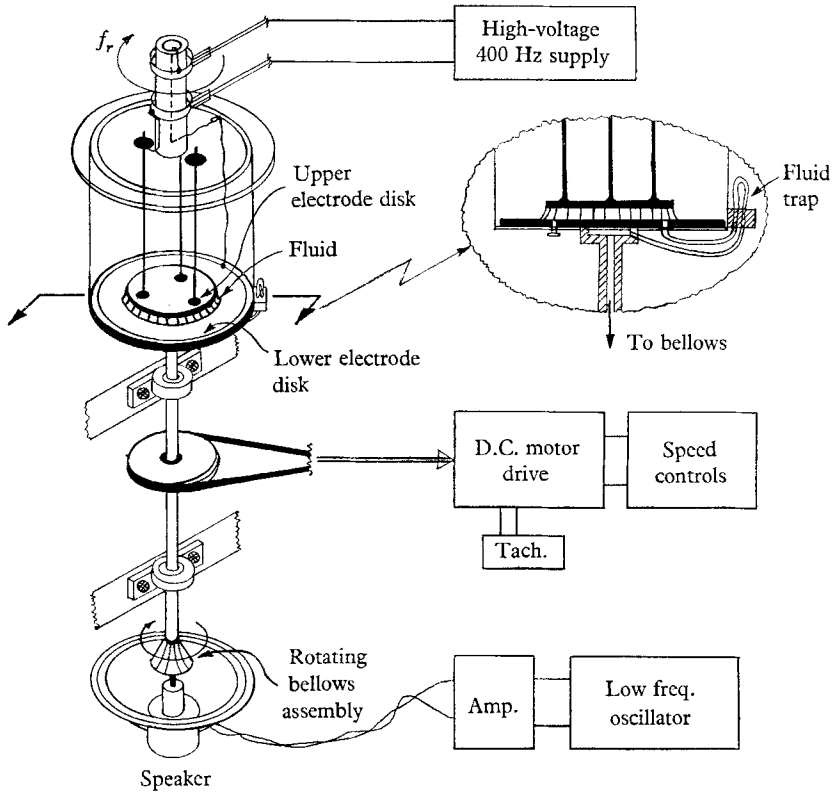

FIGURE 10. Apparatus for observation of oscillations and instability with configuration A (figure 2 (a)). The upper electrode radius $R = 8{\cdot}5$ cm and electrode spacing $a = 5$ mm or 7 mm. The rotational speed ranges from $f_r = 0 - 100$ rpm while the applied potential is 0–24 kV at 400 Hz.

of bubbles in the centre region. The electrodes are contained in a plexiglas tank which is mounted on a shroud and shaft assembly. A dc motor is geared to the shaft by means of two gear-belt reduction units, and the angular velocity is measured with a magneto-tachometer. The speed of the motor is varied from zero to 100 rpm by means of two rheostats. One of the rheostats is driven by a slow-speed ac motor and gear box for the purpose of bringing the rotating tank up to the desired velocity in a gradual and continuous manner.

The tank and drive assembly, the pressure transducer system, and the high-voltage supply are the essential components. The transducer is designed to excite the normal modes in the rotating frame of reference. A tube is introduced

through the bottom electrode into the region between the upper and lower disk electrodes, and is connected to a fluid trap, as shown. The trap likewise is connected to the hollow, vapour-filled shaft which supports the tank assembly.

At the lower end of the shaft is a rubber bellows assembly which has a thin polished disk cemented to the bottom. The bellows is driven with a loud speaker–amplifier–oscillator system by means of a plunger in contact with the polished

Mass density	$\rho = 1{\cdot}56 \times 10^3$ kg/m
Permittivity	$\epsilon = 2{\cdot}41\,\epsilon_0$
Surface tension	$T = 1{\cdot}9 \times 10^{-2}$ nt/m
Relaxation time	$\tau_r \approx 10$ sec
Viscosity	$\mu \approx 0{\cdot}6$ cp

TABLE 1. Fluid parameters for Freon 113

disk. Although the loudspeaker and plunger are fixed, the bellows assembly is free to rotate. When the transducer system is in operation, the upper connecting tubing is filled with liquid, and the remaining tubing shaft, and bellows are filled with vapour. As the tank rotates and the loudspeaker cone moves in and out with a frequency f, the plunger drives the rotating bellows in the axial direction. Thus, the rotating fluid is pulsed in the rotating frame of reference with the frequency, f, of the oscillator.

The high voltage V_0 necessary to maintain the electric field intensity $E_0 = V_0/a$ between the electrodes is transmitted through a pair of slip rings and brushes mounted on top of the rotating tank. Fields of alternating polarity which have a frequency much greater than the reciprocal relaxation time are used to avoid effects from free charges that can arise in the fluid through relaxation phenomena. Also, fluid interactions at the liquid–gas interface involving the second harmonic of the imposed fields are minimized by making the frequency high; 400 Hz is used. In computing the electrical force, the ac field is considered as a dc field having the same r.m.s. value.

For the study of oscillations and dynamic instability, it is essential that the liquid be relatively inviscid. Freon 113 is used with properties summarized in Table 1 (Du Pont Bulletin B–2 1966).

Instability

The instability experiments consist of measuring the critical voltage $V_c = E_c a$ of impending instability as a function of the rotational speed $f_r = \Omega/2\pi$ for two values of electrode separation; $a = 5$ mm and $a = 7$ mm.

The bottom electrode is covered with a layer of Freon 113. Then, with the voltage applied, the portion of the liquid under the top disk electrode becomes unstable and bridges to the disk (due to self-field effects and the perpendicular field as discussed in connexion with figure 1 (*a*)). Thus, the liquid forms a circular cylinder with an essentially vertical wall. The power supply voltage V_0 is increased to its maximum value of 24 kV to reinforce the fluid 'wall'. The tank

assembly is set in motion at a very low rotational speed, and then gradually brought up to desired speed in about 3 to 4 minutes.

When the tank has been rotating at the desired speed for a few minutes, V_0 is reduced gradually until the rotating fluid wall becomes unstable. As observed visually, the fluid bulges out slightly and then the majority of the fluid between the electrodes is ejected outward to the walls of the plexiglas tank. Occasionally, small amounts of fluid will be expelled from the rotating fluid wall at a voltage above that (V_c) at which the majority of the fluid is lost. For voltages between this 'premature' voltage and V_c the fluid is observed to be more nearly vertical.

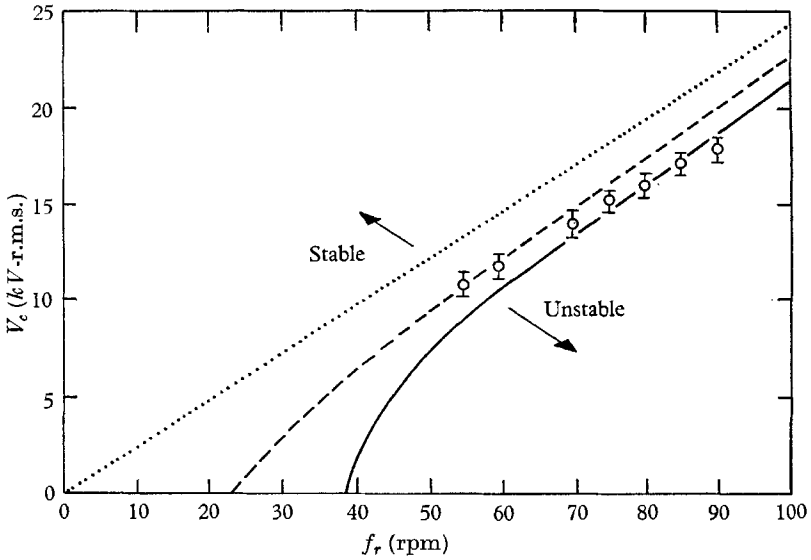

FIGURE 11. Critical voltage V_c for incipient overstability as a function of the rotational speed f_r with $a = 5$ mm. The theoretical curves show the effect of surface tension, T, on the prediction, with N a function of the wetting. Theory: ———, $N = 4$; — — —, $N = 6$; · · · · · ·, $T = 0$. Experiment: ○.

The measurements, for $a = 5$ mm, are presented in figure 11 with confidence bounds based on several repeated measurements. Similar results are found for $a = 7$ mm (Calvert 1968). Three lines indicate the predictions of (25) with surface tension effects included to various degrees. The agreement between experiment and theory is better than would be expected from the approximate nature of the simple concentrated field gradient and surface tension models. The total effect of surface tension is even less at the wider spacing of $a = 7$ mm and can be ignored for practical purposes at high values of the rotational velocities.

Normal modes

Normal mode frequencies are exhibited as the resonance frequencies of the driven fluid. These resonances are measured for the $m = 1, 2,$ and 3 modes as functions of the applied voltage for three values of rotational speed f_r. The data

are presented in figure 12 for $a = 5$ mm, with a similar result obtained for $a = 7$ mm (Calvert 1968).

Visual observations are used to identify the modes and to detect the resonances. The voltage is set at a constant value, and the frequency is increased until the first mode appears. This is detected in the laboratory frame by observing an

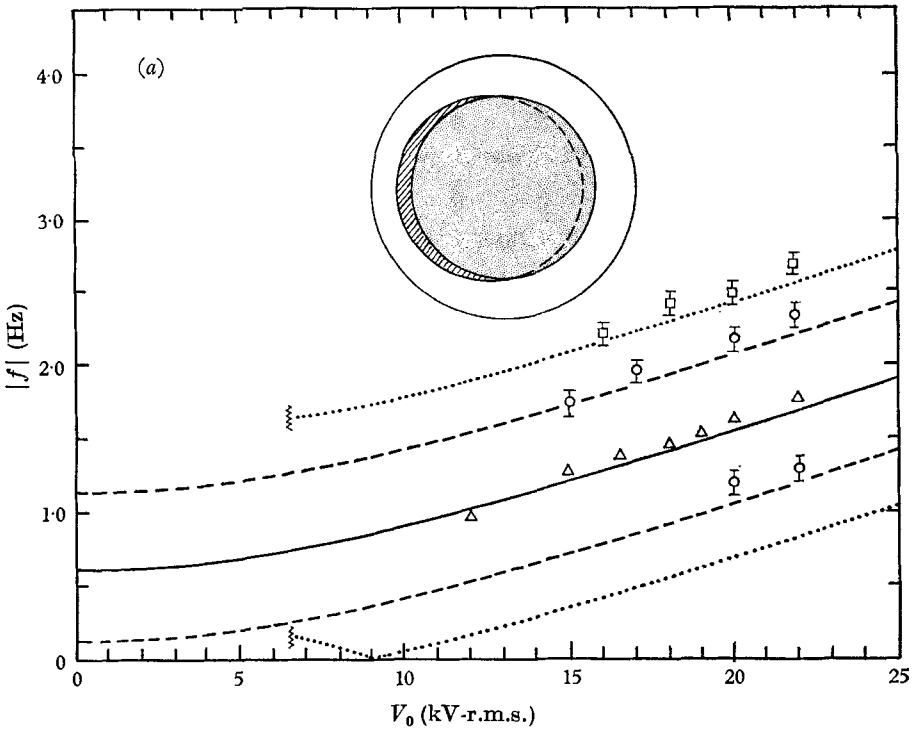

FIGURE 12. Resonance frequencies as viewed in the rotating frame for normal modes as a function of the voltage with the rotational frequency f_r as a parameter. Electrode spacing $a = 5$ mm. With $f_r = 50$ rpm, higher-order modes are unstable to the left of the point where the curves are broken off.

(*a*) $m = 1$ mode. Experiment: △, $f_r = 0$ rpm; ○, $f_r = 30$ rpm; □, $f_r = 50$ rpm. Theory: ———, $f_r = 0$ rpm; — — —, $f_r = 30$ rpm; · · · · · ·, $f_r = 50$ rpm.

(*b*) $m = 2$ mode. Experiment: △, $f_r = 0$ rpm, ○, $f_r = 30$ rpm; □, $f_r = 50$ rpm. Theory; ———, $f_r = 0$ rpm; — — —, $f_r = 30$ rpm; · · · · · ·, $f_r = 50$ rpm.

(*c*) $m = 3$ mode. Experiment: △, $f_r = 0$ rpm; ○, $f_r = 30$ rpm; □, $f_r = 50$ rpm. Theory: ———, $f_r = 0$ rpm; — — —, $f_r = 30$ rpm; · · · · · ·, $f_r = 50$ rpm.

envelope of uniform 'wobbles' on the fluid surface. As the frequency is tuned past resonance, the envelope subsides. When the frequency is further increased, the second mode appears.

The mode numbers (m) are verified in the laboratory frame of reference by viewing the fluid surface through the side of the tank, where the surface is observed to move in and out at a rate slow enough to measure with a stopwatch. This corresponds to a frequency f_l which is related to the mode number m, the

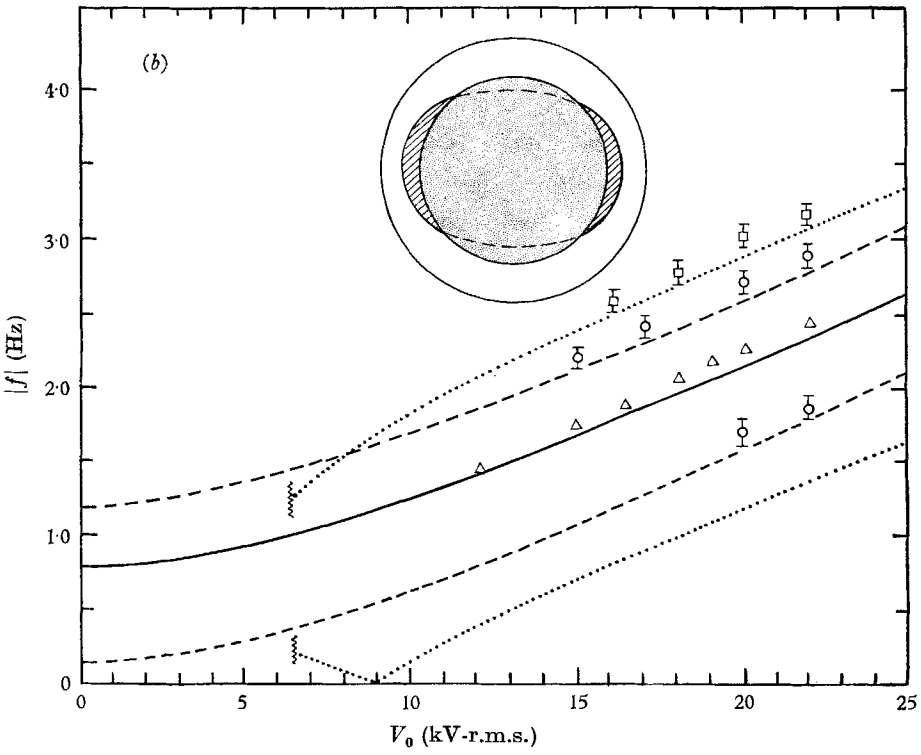

For legend see previous page.

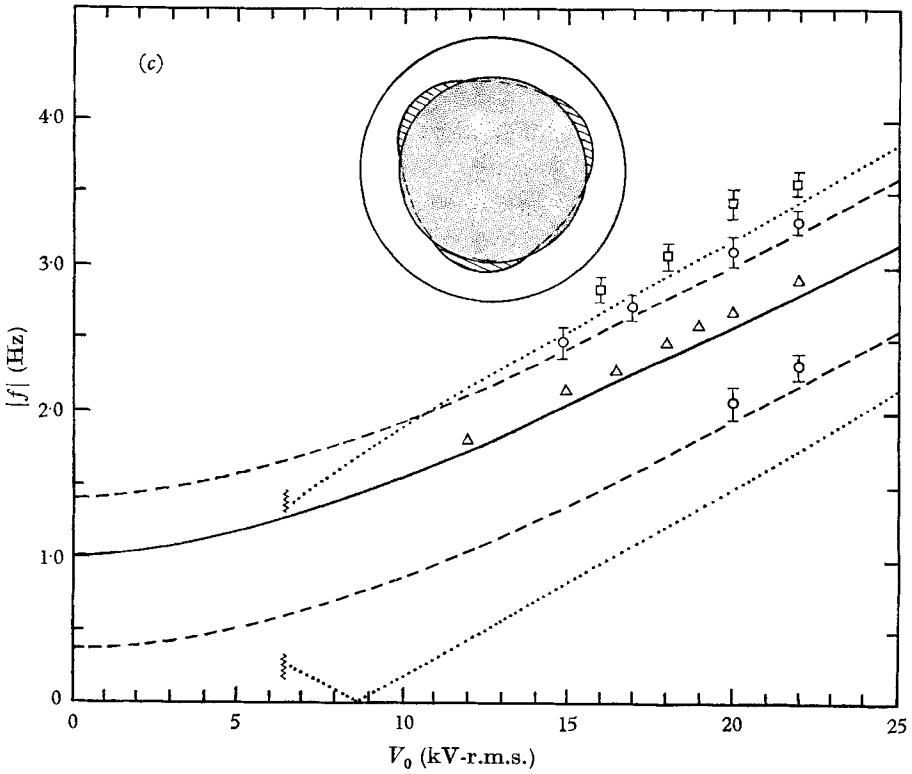

For legend see previous page.

rotational speed f_r, and the rotating frame exciting frequency $f = \omega/2\pi$ by the relation

$$|f_l| = |f| + m|f_r|. \tag{29}$$

Measurements on the lower resonance frequency of a mode pair are made using a similar technique. Low frequency data are limited due to amplifier capabilities and the difficulty of detection. However, the three lower modes are found and identified for two values of V_0 with $f_r = 30$ rpm. It is noted from (21) that the lower frequency is negative for sufficiently large E_0 and for this case (29) becomes

$$|f_l| = |f| - m|f_r|. \tag{30}$$

For experiments conducted at a speed $f_r = 50$ rpm, no reliable data are obtained for the lower frequencies due to the limitations on the exciting equipment.

The predictions based on (21) are included with figure 12. The agreement between experiment and observation lends further support to the simple quasi-two-dimensional model. For the $m = 1$ and $m = 2$ modes, the high frequency shift predictions given by (21) are found to be in excellent agreement. The $m = 3$ mode shifts are experimentally found to be somewhat greater than predicted.

Summary and further remarks

Although the addition of electric stresses to systems of rotating fluids seems at first a complication, at least for the azimuthal modes which characterize the dynamics of configuration A, the dielectrophoretic interaction makes possible a class of centrifugal modes that can be meaningfully represented by a simple model. The model is certainly simpler than that investigated by Phillips (1960) for similar ordinary centrifugal waves. This can be traced to the fact that the equilibrium is cylindrical rather than annular; the electromechanical wall makes possible modes that can be described by a single basic solution for the radial dependence of velocity. Also, self-field effects can be ignored and this reduces the representation of the electric stresses to a simple matter. The experiments support the simple model; it seems clear that the essential aspects of the dynamics in configuration A are well represented. Experimental work is called for to study configuration B, but it is not clear how effects of gravity can be removed in this case.

This work was supported by NASA Grant NGL-22-009-014.

REFERENCES

BRETHERTON, F. P., CARRIER, G. F. & LONGUET-HIGGINS, M. S. 1966 *J. Fluid Mech.* **26**, 393.

CALVERT, R. T. 1968 M.S. Thesis, Dept. of Electrical Engineering, M.I.T.

CHANDRASEKHAR, S. 1961 *Hydrodynamic and Hydromagnetic Stability*. Oxford University Press.

COWLEY, M. D. & ROSENSWEIG, R. E. 1967 *J. Fluid Mech.* **30**, 671.

DEVITT, E. B. & MELCHER, J. R. 1965 *Phys. Fluids*, **8**, 1193.

DUPONT, DE NEMOURS, E. I. & COMPANY 1966 *Freon Products Div. Technical Bulletin B-2*, Wilmington, Delaware.

FULTZ, D. 1959 *J. Meteorology*, **16**, 199.

GRODZINSKY, S. E. 1967 M.S. Thesis, Dept. of Electrical Engineering, M.I.T.

GUTTMAN, D. S. 1967 M.S. Thesis, Dept. of Electrical Engineering, M.I.T.

HABIP, L. M. 1967 *Engineering Progress at the University of Florida, XXI*, no. 2.

KELVIN, LORD 1910 *Mathematical and Physical Papers* IV, *Hydrodynamics and General Dynamics*. Cambridge University Press.

LAMB, HORACE 1932 *Hydrodynamics*. New York: Dover.

LIGHTHILL, M. J. 1966 *J. Fluid Mech.* **26**, 411.

MELCHER, J. R. 1963 *Field-Coupled Surface Waves*. Cambridge, Mass: MIT Press.

MELCHER, J. R., GUTTMAN, D. S. & HURWITZ, M. 1969 *J. Spacecraft and Rockets*, **6**, 25.

MELCHER, J. R. & HURWITZ, M. 1967 *J. Spacecraft and Rockets*, **4**, 864.

MELCHER, J. R., HURWITZ, M., FAX, R. G. & BLUTT, J. 1969 *J. Spacecraft and Rockets*. (To be published.)

MELCHER, J. R. & SCHWARTZ, W. J. 1968 *Phys. Fluids*, **11**, 2064.

NAYYER, N. K. & MURTY, G. S. 1960 *Proc. Phys. Soc.* **75**, 369.

PHILLIPS, O. M. 1960 *J. Fluid Mech.* **7**, 340.

REYNOLDS, J. M. 1965 *Phys. Fluids*, **8**, 161.

ROUSE, H. 1946 *Elementary Mechanics of Fluids*. New York: Wiley.

STRATTON, J. A. 1941 *Electromagnetic Theory*. New York: McGraw-Hill.

WONG, J. 1966 B.S. Thesis, Department of Electrical Engineering, M.I.T.